Delft University of Technology

Cavitation erosion risk assessment on a full-scale steerable thruster

Melissaris, Themistoklis; Schenke, Sören; Bulten, Norbert; van Terwisga, Tom J.C.

Important note
To cite this publication, please use the final published version (if applicable).
Please check the document version above.

Cavitation erosion risk assessment on a full-scale steerable thruster

Themistoklis Melissaris [a,b,*], Sören Schenke [a], Norbert Bulten [b], Tom J.C. van Terwisga [a,c]

[a] *Delft University of Technology, The Netherlands*
[b] *Wärtsilä Netherlands BV, The Netherlands*
[c] *Maritime Research Institute Netherlands, The Netherlands*

ABSTRACT

Propeller cavitation erosion prediction at an early design stage is becoming more and more important since it is one of the key constraints in the search for maximum propeller efficiency. Despite the experience from model tests, cavitation erosion research on actual ship scale is very limited. In this study, an attempt is made to assess the erosion risk on the blades of a full-scale steerable thruster of a tug boat. Pressure side cavitation was detected on board for three different propeller designs. For the first time, a cavitation erosion analysis is performed on ship-scale, using a rigorous potential energy approach, which accounts for the focusing of the potential energy at the collapse center during the cavity collapse. A full sensitivity study has been performed for the blade surface accumulated energy. The erosion model shows the erosion risk for different propeller designs applied on the vessel, and different operating conditions, by looking at the surface specific energy on the blade. The erosion analysis shows locations of high erosion risk that show a good resemblance with the actual damage locations on the real blades.

1. Introduction

Cavitation is characterized by the sudden growth and intense collapse of vapor structures in a liquid due to large pressure variations. Vaporization of a liquid occurs when its pressure drops below the vapor pressure, while when these vapor structures enter a pressure recovery region they collapse. The intensity of their collapse depends strongly on the pressure difference they are subjected to, and the collapse may be so violent that can result in undesired nuisance such as noise, vibrations, and erosion damage. While noise and vibrations are most of the times acceptable until a certain level, cavitation erosion should be avoided, since severe erosion on mechanical components such as propellers, pumps, valves etc. has a significant impact on their efficiency and structural integrity.

Efficient propeller designs cavitate and there is a trade-off between hydrodynamic efficiency and cavitation (Carlton, 2019; Chahine et al., 2014). Therefore cavitation on the propeller blades is most of the times unavoidable. However, there is a limit until a propeller can cavitate without eroding (or eroding with a very small erosion rate), resulting in the maximum hydrodynamic efficiency. This limit is hard to predict and identify. Cavitation observations in a towing tank using high speed cameras are conducted conventionally to get an impression of the erosiveness of the cavitating structures on the blades in model-scale. Although, such observations can give important information about the shape of the cavity, and possible locations of collapses, it is hard to

quantify the intensity and violence of a collapse, while the influence of scale effects is also not considered. Furthermore, propeller designers are using potential flow codes to optimize any propeller design. The majority of those potential flow models, cannot represent the break-up of cavities, and certainly not the dynamics of their collapse. These aspects lead to the necessity of a numerical tool which can simulate the growth and collapse of such cavitating structures on the blade and assess the intensity and aggressiveness of their collapse, as well as the surface impact distribution, with sufficient accuracy.

Although cavitation dynamics have been thoroughly investigated during the last decades, cavitation erosion prediction on marine propellers still remains a challenging topic. And while there are several studies in model scale, investigations on full scale propellers are very limited. In one of the first attempts to predict cavitation erosion on ship scale, Ponkratov and Caldas (2015) and Ponkratov (2015), estimated cavitation aggressiveness on the rudder and the propeller, respectively. The results showed good correlation with the actual eroded areas. They used erosion functions developed by the Lloyd's Register Technical Investigation Department (LR TID), however these functions have not been reported in the studies. Peters et al. (2018) used the micro-jet hypothesis to predict cavitation erosion on a ship propeller, both in model and full scale. The simulations were compared to experimental data, demonstrating a good qualitative prediction of the cavitation erosion on the propeller.

Nomenclature

Subscripts

0	Initial
C	Condensation
pot	Potential
rad	Radiated
reb	Rebound
SW	Shock wave
v	Vapor/evaporation
cell	Cell (center)
S	Surface

Nomenclature

α	Volume fraction (-)
β	Collapse parameter (-)
τ	Viscous shear stress tensor (Pa)
$\mathbf{u}_i$	Collapse induced velocity (m/s)
$\mathbf{u}$	Flow velocity vector (m/s)
$\mathbf{x}$	Location vector (m)
$\delta t, \Delta t$	Time increment, simulation time step size (s)
ΔU	Internal energy (J)
$\mathbf{r}$	Position vector
$\mathfrak{P}_b(a)$	Normalized projection of vector $\mathbf{a}$ on vector $\mathbf{b}$ such that $\mathfrak{P}_b(a) = \frac{\mathbf{a} \cdot \mathbf{b}}{\|a\| \|b\|}$
μ, μ_l, μ_v	Turbulent eddy viscosity of mixture, liquid, vapor (kgs/m^2)
Ω	Solid angle (sr)
ϕ	Spatial transport operator
ρ, ρ_l, ρ_v	Density of mixture, liquid, vapor (kg/m^3)
θ, ϕ	Polar, azimuthal angle in spherical coordinates (deg)
ε	Collapse induced kinetic energy per volume
A_f	Face area (m^2)
c	Minimum cell size (mm)
D	Propeller diameter (m)
d, ∂, D	General, partial, material derivative operator
E	Energy (J)
e	Energy per volume (J/m^3)
f	External force per unit mass (N/kg)
h_i, h_3	Typical cell size of grid i, grid 3
p, p_d, p_v	Absolute, driving, vapor pressure (Pa)
P_d	Delivered power (kW)
r	Sphere radius (m)
S_{α_v}	Mass transfer source term (1/s)
T	Vessel draught (m)
t, τ, T, T_m	Time, collapse time, sample time, moving time window (s)
V	Volume (m^3)
z	Z-coordinate of the propeller center from the baseline (m)

The limited research on ship scale propeller erosion prediction emphasizes the difficulty of performing such simulations, as well as the necessity of a more reliable and quantitative approach. In this study, an attempt exactly towards this step is made, where a more quantitative prediction of the cavitation erosion risk on the propeller blades is pursued. We compute the cavitation impact loads on the blades of a full-scale steerable thruster propeller. The erosion risk is represented by the surface specific energy distribution on the blade area, originated from the implosion of the cavitating structures. An energy balance approach is employed (Fortes-Patella and Reboud, 1998; Flageul et al., 2012; Fortes-Patella et al., 2013), where we allow for the focusing of the potential energy, contained in the cavitating structures, into the collapse center, before it is radiated in a shock wave.

At the moment of a cavity collapse, energy is emitted isotropically in the domain. The computation of the exact amount of the radiated energy that will reach any surface in the vicinity, involves the concept of the solid angle. A solid angle is a 3D angular volume that is defined analogously to the definition of a plane angle in two dimensions (Arecchi et al., 2007). In this study, a fully continuous reconstruction of the solid angle is used. For unstructured meshes, the analytical computation of the solid angle is not straightforward, and a discrete approximation is often used instead. For sources very close to the surface, this approximation leads to solid angles significantly larger than the exact solid angle, leading to substantial errors in the computation of the surface accumulated energy. To minimize these errors, the solid angle is bounded to its maximum value.

Finally, to assess the reliability of the model on full scale simulations, an extensive verification study has been performed, based on propeller designs which have been in real operation. The results of the CFD simulations are validated against the actual eroded areas on the used azimuth-thruster propeller blades.

2. Numerical modeling

2.1. Governing equations and cavitation modeling

The Reynolds Averaged Navier–Stokes (RANS) equations for momentum and mass continuity are solved, given by

$$\frac{\partial(\rho \mathbf{u})}{\partial t} + \nabla \cdot (\rho \mathbf{u}\mathbf{u}) = -\nabla p + \rho f + \nabla \cdot \tau \qquad (1)$$

$$\frac{\partial \rho}{\partial t} + \nabla \cdot (\rho \mathbf{u}) = 0 \qquad (2)$$

where $\mathbf{u}$ is the velocity tensor, ρ is the fluid density, p the pressure, f the external force per unit mass and τ the viscous part of the stress tensor. The density and the turbulent viscosity of the cavitating flow is given by the mixture relations

$$\rho = a_v \rho_v + (1 - a_v)\rho_l \qquad and \qquad \mu = a_v \mu_v + (1 - a_v)\mu_l \qquad (3)$$

respectively, where $0 < a_v < 1$ is the vapor fraction. The phase transition is modeled using a homogeneous multiphase mixture model. A single set of momentum equations is solved for the mixture. An additional transport equation is solved to determine the volume fraction of each phase in each computational cell

$$\frac{\partial \alpha_v}{\partial t} + \nabla \cdot (\alpha_v \mathbf{u}) = S_{\alpha_v} \qquad (4)$$

where S_{α_v} is the mass transfer source term, modeled by the Schnerr–Sauer cavitation model. For further details see Melissaris et al. (2019, 2020).

The k-ω SST turbulence model by Menter (1994) is used to model the Reynolds Stress term. A finite-volume discretization technique with cell centered collocated variables is employed to solve the equations. The governing equations are solved sequentially in a segregated manner. The mass conservation is ensured by a pressure correction equation based on the SIMPLE (**S**emi-**I**mplicit **M**ethod for **P**ressure-**L**inked **E**quations) algorithm (Patankar, 1980). To avoid the artificial increase of eddy viscosity at the mixture regime, an empirical reduction of turbulent dissipative terms is applied, by modifying the turbulent eddy viscosity (see Melissaris et al., 2019)

2.2. Cavitation erosion modeling

Cavitation erosion is modeled considering an energy transfer from the collapsing cavitating structures to the impacted surface. The approach is based on the potential energy hypothesis (Hammit, 1963; Vogel and Laterborn, 1988) where the potential energy, initially contained in the vapor cavities, is proportional to the pressure difference driving the cavity collapse $p_d - p_v$, and the cavity vapor volume V_v. During the collapse, the initial potential energy can be partitioned into different forms of energy, and the instantaneous energy balance is considered (Obreschkow et al., 2006; Tinguely et al., 2013). The initial potential energy is first converted into kinetic energy, before it is radiated in the domain as acoustic (shock wave) energy. For strong inertia driven flows (about 1 bar driving pressure difference $p_d - p_v$ or higher), and in the absence of non-condensible gas within the cavitating structures, any thermal effects and cavity rebounds respectively, may be neglected (Tinguely et al., 2013). Thus, at the final stage of the collapse, all the initial potential energy has been converted into shock wave energy:

$$E_{SW} = E_{pot,0} - E_{reb} - \Delta U \xleftrightarrow{\quad E_{reb} \approx 0, \ \Delta U \approx 0 \quad} E_{SW} \approx E_{pot,0}$$
(5)

In every computational cell, the instantaneous volume specific change of potential energy is given by

$$\dot{e}_{pot} = \frac{DE_{pot}/Dt}{V_{cell}} = (p_d - p_v) \cdot \frac{D\alpha_v}{Dt} + \frac{Dp_d}{Dt} \cdot \alpha_v$$
(6)

In Eq. (6) only the first term on the r.h.s. can directly feed into collapse induced kinetic energy, as it represents the change of potential energy due to condensation or evaporation. The second term describes any change of potential energy due to changes of the ambient pressure, however this change can only contribute to inertial motion of the cavities, and it does not involve any change in the vapor volume and subsequently to the collapse induced velocity field around the cavities (see Melissaris et al., 2020; Schenke, 2020).

Combining Eqs. (3), (4) and (6), and considering only condensation, the volume specific potential energy reduction rate becomes

$$\dot{e}_{pot,C}(t, \mathbf{x}_{cell}) = (p_d - p_v) \cdot min \left[\frac{\rho}{\rho_l} S_{\alpha_v}, 0 \right]$$
(7)

In Eq. (7) the condensation rate is computed from the cavitation mass transfer model source term S_{α_v}, as in previous work it has been shown that the error made in the reconstruction of the material derivative of the vapor volume, $D\alpha_v/Dt$, is then minimized (see Melissaris et al., 2020). The driving pressure field p_d, is computed by time-averaging the instantaneous pressure field in cavitating conditions, p, over one shedding period of the cavity cycle (or higher) (Melissaris et al., 2020; Schenke et al., 2019a). To avoid exceeding random-access memory (RAM) limits, the method applied by Welford (1962) is used to approximate the moving average of the instantaneous pressure field, $\bar{p}_t$, at time instant t, at each computational cell:

$$\bar{p}_t = \bar{p}_{t-1} + \left(p_t - \bar{p}_{t-1} \right) \frac{\Delta t}{T_m}$$
(8)

where Δt is the time step size, and T_m the sliding window, equal to the cavity shedding period (or higher).

To account for energy partition during the condensation process, a transport equation is implemented for the collapse induced kinetic energy ε, which is given by Schenke (2020)

$$\frac{\partial \varepsilon}{\partial t} + \mathbf{u}_i \cdot \nabla \varepsilon = -\varepsilon(\nabla \cdot \mathbf{u}_i) - \dot{e}_{rad}(t)$$
(9)

where $\mathbf{u}_i$ is the collapse induced velocity. The terms $\varepsilon(\nabla \cdot \mathbf{u}_i)$ and $\dot{e}_{rad}(t)$ of Eq. (9) represent the conversion of the potential energy into collapse induced kinetic energy and the conversion of the kinetic energy to radiated acoustic energy, respectively. The term $\mathbf{u}_i \cdot \nabla \varepsilon$ represents

the conservative advective transport of ε, however the distribution of the collapse induced kinetic energy during the cavity collapse is not known, and therefore a modeling assumption is introduced. In previous work (Schenke et al., 2019b; Melissaris et al., 2020; Schenke, 2020), we have shown that the collapse induced kinetic energy transport (Eq. (9)) can be modeled as

$$\frac{\partial \varepsilon}{\partial t} = (1 - \beta)[\phi(\varepsilon) - \dot{e}_{pot,C}(t)] - \beta \frac{\varepsilon}{\delta t}$$
(10)

where $\phi(\varepsilon)$ is a model for the advective transport of the kinetic energy, and $\dot{e}_{pot,C}(t)$ is the reduction of potential energy. The parameter β is responsible for the conversion of the collapse induced kinetic energy into acoustic radiated energy, and it is defined as follows:

$$\beta = \begin{cases} 1, & if \quad p > p_\infty \quad and \quad \alpha = 0 \\ 0, & else \end{cases}$$
(11)

When $\beta = 0$, then potential cavity energy is being converted into collapse induced kinetic energy, while when $\beta = 1$ the kinetic energy, focused at the cavity collapse center, is released as shock wave energy.

The conservative transport of the induced kinetic energy, $\phi(\varepsilon)$, can be decomposed into a production and a reduction term, such that

$$\int_V \left[\phi(\varepsilon)^+ + \phi(\varepsilon)^- \right] dV = 0$$
(12)

The production and reduction terms are defined as

$$\phi(\varepsilon)^+ = -k\dot{e}_{pot,C}(t, \mathbf{x}_{cell}), \quad where \quad k = \begin{cases} \dfrac{\displaystyle\int_V \phi(\varepsilon)^- dV}{\displaystyle\int_V \dot{e}_{pot,C}(t) dV}, & for \quad \dot{e}_{pot,C} < 0 \\ \\ 0, & elsewhere \end{cases}$$
(13)

and

$$\phi(\varepsilon)^- = -\frac{\varepsilon}{\delta t} \mathfrak{P}_u(\nabla \varepsilon)$$
(14)

,respectively. In Eqs. (13) and (14), $\mathfrak{P}_u(\nabla \varepsilon)$ is the normalized projection of $\nabla \varepsilon$ on the local flow velocity vector $\mathbf{u}$

$$\mathfrak{P}_u(\nabla \varepsilon) = \max \left[\frac{\mathbf{u}}{\|\mathbf{u}\|} \cdot \frac{\nabla \varepsilon}{\|\nabla \varepsilon\|}, 0 \right]$$
(15)

Then, the transport equation of ε given by Eq. (10) becomes

$$\frac{\partial \varepsilon}{\partial t} = (1 - \beta) \left[\dot{e}_{pot,C}(k - 1) - \frac{\varepsilon}{\delta t} (\mathfrak{P}_u(\nabla \varepsilon)) \right] - \beta \dot{e}_{rad}$$
(16)

Forwarding the solution in time gives the collapse induced kinetic energy at each time step Δt

$$\varepsilon|_{t+\delta t} = \varepsilon|_t + \frac{\partial \varepsilon}{\partial t}\bigg|_t \delta t = (1 - \beta|_t) \left[\dot{e}_{pot,C} \delta t(k - 1) - \varepsilon(\mathfrak{P}_u(\nabla \varepsilon) - 1) \right]\bigg|_t$$
(17)

and the volume specific radiated power is given by

$$\dot{e}_{rad}|_{t+\delta t} = \frac{1}{\delta t} (\beta \varepsilon)|_t$$
(18)

A more detailed description and implementation of the model can be found in Schenke (2020), and Melissaris et al. (2020).

2.3. Surface impact power

When a cavitating structure has fully collapsed, it is assumed that all the initial potential energy contained in the structure has been converted into shock wave energy. This energy is emitted from the source (collapse point) isotropically. The energy is radiated instantaneously to any surrounding surface, which means that the propagation speed is infinite. The simplifying assumption of infinite wave propagation speed is justified by the fact the advective velocities are typically orders of magnitude smaller than the sound speed in a nearly incompressible medium such as water. The fraction of energy which passes through any surface is simply the solid angle Ω subtended by this surface at
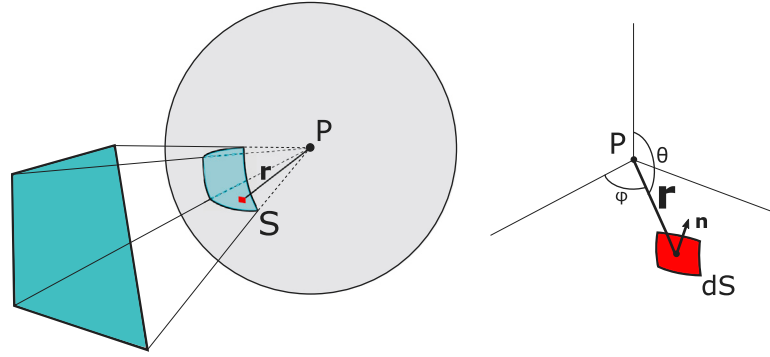
Fig. 1. Representation of the solid angle for an arbitrary oriented surface subtended to a point P. The solid angle of that surface is equal to the solid angle of its projection S to the unit sphere with center P, and radius r.
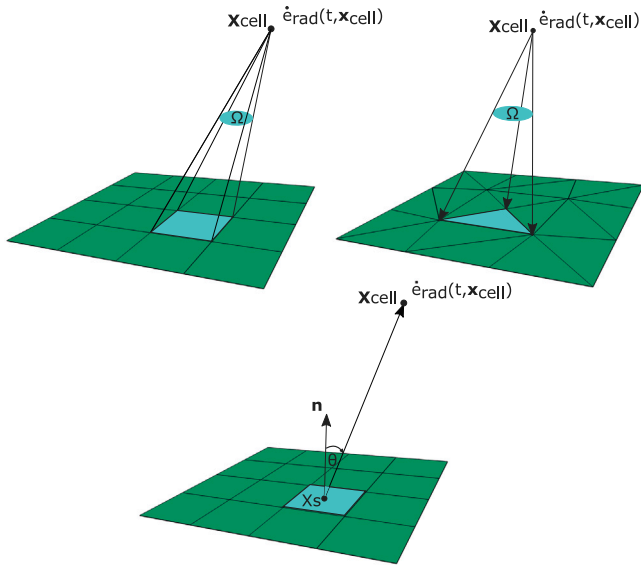

Fig. 2. Solid angle for a rectangular (top left) and triangular surface (top right), and a surface face center (bottom) subtended to a radiation source at a volume cell center $\mathbf{x}_{cell}$.

the source point, divided by the total solid angle (Rowlands, 1961). In such way, we quantify the distance and angle dependencies. For a closed convex surface, $\Omega = 4\pi$, and thus, the impact power on a surface location $\mathbf{x}_S$ at time instant t is given by

$$\dot{e}_S(t, \mathbf{x}_S) = \frac{\Omega}{4\pi} \dot{e}_{rad}(t, \mathbf{x}_{cell}) \tag{19}$$

where $\dot{e}_{rad}(t, \mathbf{x}_{Cell})$ is the radiated power at a volume cell center $\mathbf{x}_{Cell}$. By definition, the solid angle for an arbitrary oriented surface subtended at a point P is equal to the solid angle of the projection of the surface to the unit sphere with center P (see Fig. 1), and it is given by

$$\Omega = \iint_S \frac{\hat{r} \cdot \mathbf{n}}{\|\mathbf{r}\|^2} dS = \iint_S \frac{\mathbf{r} \cdot \mathbf{n}}{\|\mathbf{r}\|^3} dS = \iint_S \sin\theta d\theta d\phi \tag{20}$$

where for an infinitesimal area dS, $\mathbf{r}$ is the position vector with respect to P, and $\mathbf{n}$ the unit normal vector. θ and ϕ are the polar and azimuthal angle in spherical coordinates respectively.

Using Eq. (20) Gotoh and Yagi (1971) were able to derive analytically the solid angle subtended by a rectangle to an arbitrary point. In a similar way, Oosterom and Strackee (1983) used an analytic exact expression of the solid angle for a plane triangle, which was used by Leclercq et al. (2017) to deduce the rate of impact energy applied on the surface (see Fig. 2). However, both cases require to discretize the surface into rectangular and triangular elements of finite

size respectively. For complicated geometries, where unstructured grids are predominantly used, this is not always straightforward. In this respect, Schenke et al. (2019b) proposed a fully continuous form of the solid angle, that represents the impact at a surface point location. Then, a discrete formulation of the solid angle Ω_d for any surface location $\mathbf{x}_S$ subtended to a volume cell center $\mathbf{x}_{cell}$ is given by

$$\Omega_d = \frac{(\mathbf{x}_{cell} - \mathbf{x}_S) \cdot \mathbf{n}}{\|\mathbf{x}_{cell} - \mathbf{x}_S\|^3} A \approx \frac{(\mathbf{x}_{cell} - \mathbf{x}_S) \cdot \mathbf{n}}{\|\mathbf{x}_{cell} - \mathbf{x}_S\|^3} A_f \tag{21}$$

In Eq. (21), A is the area of the projection of the surface face to a sphere with center $\mathbf{x}_{cell}$ and radius $\|\mathbf{x}_{cell} - \mathbf{x}_S\|$. Since this projected area is not known, and for arbitrary surfaces is hard to compute, we can substitute the projected area with the face area A_f. This leads to an approximation of the discrete solid angle Ω_d, which can be applied however, to any surface subtended to any arbitrary point.

However, the error involved in the discrete approximation of the solid angle, can be significant for large solid angles, as it strongly depends on the location of the point source and its distance from the surface face, as illustrated in Fig. 3. The solid angle Ω_1 of a flat surface with face area A_f subtended to a point $\mathbf{x}_{P_1}$ with position vector pointing in the same direction as the surface normal vector, is equal to

$$\Omega_1 = \frac{(\mathbf{x}_{P_1} - \mathbf{x}_S) \cdot \mathbf{n}}{\|\mathbf{x}_{P_1} - \mathbf{x}_S\|^3} A_1 = \frac{A_1}{r_1^2} \tag{22}$$

where A_1 the area of the surface projection to a sphere with radius r_1, and the error made in the discrete approximation of the solid angle is represented by the ratio A_1/A_f. The further from 1 the ratio, the larger the error. When the source is closer to the surface ($r_2 < r_1$), the solid angle increases ($\Omega_2 > \Omega_1$), while the projected area decreases ($A_2 < A_1$). Thus, for larger solid angles, the error increases. When the source is extremely close to the surface the discrete approximation of the solid angle can lead to solid angles orders of magnitude larger than the maximum solid angle ($\Omega_{max} = 2\pi$ for a flat surface subtended to a point). One way to minimize the margin of error is to bound the solid angle to always be smaller or equal to 2π such that

$$\Omega_d = min \left[\left(\frac{(\mathbf{x}_{cell} - \mathbf{x}_S) \cdot \mathbf{n}}{\|\mathbf{x}_{cell} - \mathbf{x}_S\|^3} A_f \right), 2\pi \right] \tag{23}$$

If the approximation error still remains significant, the surface face could further be discretized into smaller equal segments, and then the discrete solid angle could be computed for each segment, resulting in an error reduction proportional to the ratio of the initial face area over the new face area. If the surface face is known a priori to be rectangular or triangular, then the exact analytical solution for the solid angle can be used.

Now, considering all the emission sources, the impact power per unit surface at any location $\mathbf{x}_S$ is given by

$$\dot{e}_S(t, \mathbf{x}_S) = \frac{1}{4\pi A_f} \int_V \Omega_d \, \dot{e}_{rad}(t, \mathbf{x}_{cell}) dV \tag{24}$$
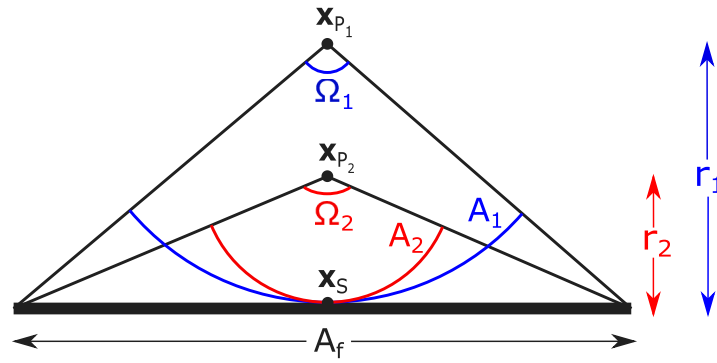
Fig. 3. Solid Angles of a flat surface subtended to the points $\mathbf{x}_{P_1}$ and $\mathbf{x}_{P_2}$, where r_1 and r_2 are the distances of $\mathbf{x}_{P_1}$ and $\mathbf{x}_{P_2}$ from the face center $\mathbf{x}_S$, respectively, with $r_1 > r_2$.

Table 1
Operating conditions reported responsible for high cavitation erosion risk on the propeller blades.

Condition	% of time	Power [kW]	Vessel speed [kn]	Propeller revs [RPM]	Draught [m]
Ballast min load	1%	1000 (33%)	7	217.7	4.5
Minimum towing	48%	1000 (33%)	0	217.7	5.2
Dynamic positioning	7%	600 (20%)	0	217.7	5.2

and the accumulated surface specific energy e_S at any location $\mathbf{x}_S$ and after some sample time T is given by

$$e_S(T, \mathbf{x}_S) = \int_0^T \dot{e}_S(t, \mathbf{x}_S) dt \tag{25}$$

Finally, integrating over the surface gives the total accumulated surface energy after some sample time T

$$E_S(T) = \int_S e_S(T, \mathbf{x}_S) dS \tag{26}$$

3. Test case description

A Tug boat is a type of vessel that maneuvers other vessels by pushing or pulling. As a result, these type of vessels operate at low speeds for long periods of time. The test case considered in this study is a tug boat equipped with two steerable propulsion thrusters. The thrusters operate at constant rotation rate, and the propeller thrust (and therefore various vessel speeds) for different conditions is achieved by adjusting the propeller pitch. The original propeller design of the thrusters, first mounted on the ship, experienced extensive pressure side cavitation at certain conditions, leading to severe cavitation erosion on the blades. The first attempt to improve the propeller design was followed by a reduced amount of pressure side cavitation on the blades at the same critical conditions. Nevertheless, the propeller blades still suffered from cavitation erosion, even though the actual erosion rate was observed to be lower. Finally, a third propeller was designed, which showed the least amount of pressure side cavitation at the critical conditions, and the erosion rate on the blades was minimized. Table 1 shows the critical operating conditions, and the three different propeller designs are depicted in Fig. 4.

To reduce the computational cost, the flow towards the thruster unit is simulated without including the ship hull, since it is assumed that the unit itself is mainly responsible for the non-uniform inflow to the propeller. Fig. 5 shows the computational domain. The top boundary is located at the waterline level, which is at distance $T - z_{prop}$ from the propeller center, where T is the draught of the vessel, and z_{prop} the z coordinate of the propeller center from the baseline. A symmetry plane is applied on the top boundary. The (velocity) inlet and the (pressure) outlet are located 6 diameters from the propeller center, while the side (slip) walls and the bottom boundary (symmetry plane) are 3 diameters away from the propeller center.
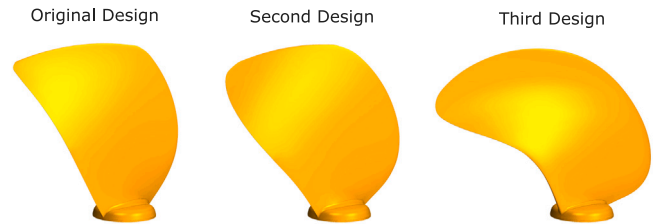

Fig. 4. Original propeller design (left), and first (middle) and second (right) redesigns.
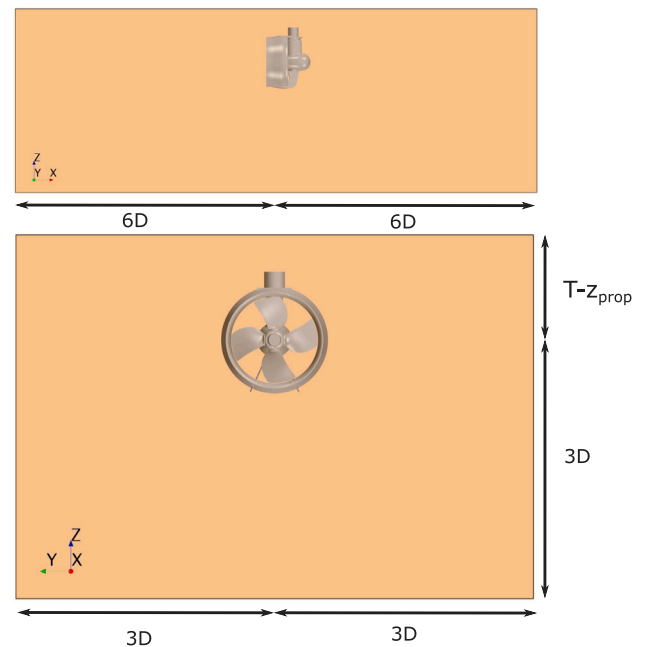

Fig. 5. Representations of the computational domain D2, and the location of the thruster unit. The propeller is rotating in clockwise direction seen from the aft.
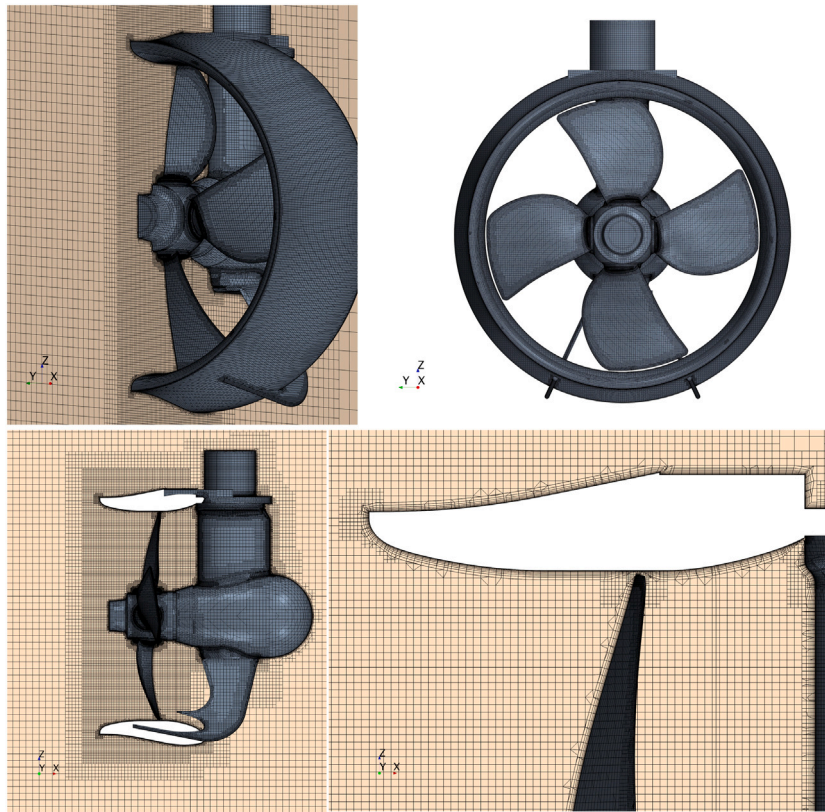
Fig. 6. The finest (Grid 3) mesh around the Nozzle and Propeller.

4. Power prediction

To simulate the performance of the thruster, the generated mesh consists of trimmed hexahedral cells with local refinements and prism layers along the wall boundaries. Wall functions are used to model the near wall region, applying 8 prism layers, and a first cell distance resulting in wall y^+ values so that $30 < y^+ < 300$. A moving mesh with sliding interfaces is employed to simulate the propeller motion. The moving grid area is determined by a second domain around the propeller geometry (spin domain). A representation of the mesh around the propulsion thruster is depicted in Fig. 6. The computational results can sometimes be highly dependent on the size of this spin domain, especially for nozzle propellers, due to the restrictions on the size imposed by the geometry itself. Thus, a sensitivity study needs to be conducted, apart from the time step and grid size investigation.

4.1. Sensitivity study

A verification study is conducted to investigate the sensitivities related to the outer domain size, the spin domain size, the time step size, and the grid density. Three domain sizes have been used to assess the influence of the boundaries to the solution. Apart from the medium domain size, D2, shown in Fig. 5, two more have been tested, one with dimensions two time smaller, D1, and one with dimensions 5 time larger, D3. Of course, the distance from the free surface remains the same for all three domains. Table 2 presents the difference in power predictions for the three domain sizes. Delivered power is 1.4% higher for the smallest domain compared to the largest one, while for the medium domain size the difference is less than 0.5%. In order to reduce the number of cells and therefore CPU time, the medium domain size has been selected for all the calculations.

The size of the spin domain is determined by the location of the interface at the inflow and the outflow of the moving mesh. The

Table 2
Delivered power for three different outer domain sizes for Grid 3 for the original blade, pitch deflection −11 deg at the ballast minimum load condition.

Outer domain	Power [kW]	Deviation from D1
D1	940.4	1.40%
D2	931.6	0.49%
D3	927.1	–

interfaces should be located at areas with low velocity and pressure gradients. However, very often geometrical restrictions impose certain limits to the size of the spin domain and the location of the interfaces. In this particular case, the location of the inflow interface is limited by the connections between the pod and the nozzle. Thus, the inflow interface is positioned as far from the propeller blades as possible, but cannot extend further than the connections at the inner part of the nozzle (see Fig. 7). On the other hand, the location of the outflow interface is not limited by any geometrical part, and thus the optimum size has been investigated.

Four different spin domain sizes are tested, as shown in Fig. 8. The first spin domain is the smallest and it includes the blade, the hub and part of the hubcap. The second spin domain includes the whole hubcap, the third spin domain is extended until the trailing edge of the nozzle, and the fourth spin domain is extended even further away than the nozzle trailing edge. Table 3 shows the thruster power output for each spin domain size. When the spin domain is extended until the nozzle trailing edge or further, then the delivered power P_d is independent of the domain size.

The delivered power P_d is calculated for the finest grid (Grid 3) and four different time step sizes 1,2,4 and 8 deg per time step (see Table 4). The results seem to be time step independent even for the highest time step size (8 deg per time step). Furthermore, Table 5 shows
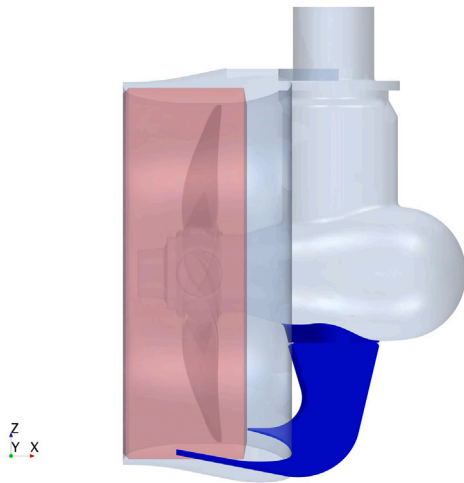
Fig. 7. Geometrical restriction on the size of the spin domain, where it extends until the connection between the thruster pod and the inner part of the nozzle.
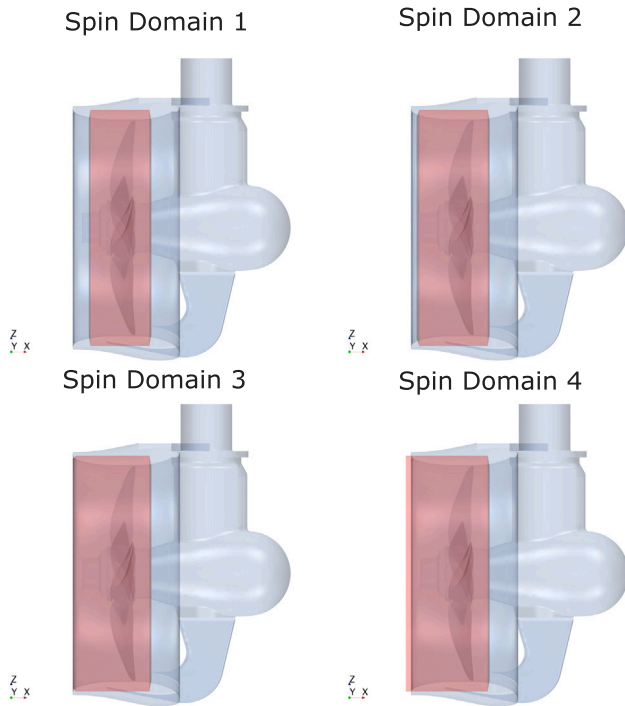

Fig. 8. Spin Domain Size.

Table 3
Delivered power for different spin domain sizes for Grid 3 for the original blade, pitch deflection −11 deg at the ballast minimum load condition.

Spin domain	Power [kW]	Deviation from SD4
SD1	940.4	0.94%
SD2	933.7	0.21%
SD3	931.6	0.01%
SD4	931.7	–

the delivered power P_d, as calculated for three different grid densities, and for a time step size of 1 deg per time step. Since wall functions are used to model the near wall region, the same prism layer mesh has been used for all grids, to keep the same $y+$ values for a more fair comparison. It has been shown that even the coarsest grid is sufficiently

Table 4
Delivered power for different time step sizes for Grid 3 for the original blade, pitch deflection −11 deg at the ballast minimum load condition.

Rotation rate	Power [kW]	Deviation from 1 deg/Δt
8 deg/Δt	931.3	−0.03%
4 deg/Δt	930.1	−0.17%
2 deg/Δt	929.6	−0.22%
1 deg/Δt	931.6	–

Table 5
Delivered power for different grid densities, for the original blade, pitch deflection −11 deg, and time step size 1 deg/Δt, at the ballast minimum load condition.

	# Cells (10^6)	h_i/h_3	Power [kW]	Deviation from grid 3
Grid 1	5.26 M	1.5625	926.1	−0.59%
Grid 2	6.53 M	1.25	932.1	0.05%
Grid 3	9.06 M	1	931.6	–

Table 6
Propeller pitch deflection for each blade design and each operating condition.

Condition	Power (kW)	Pitch deflection (deg)		
		1st design	2nd design	3rd design
BML	1000	−10.41	−5.90	–
MT	1000	−12.35	−8.09	–
DP	600	−17.68	−12.71	−13.61

fine, as far as the delivered power P_d is concerned. The deviation of the delivered power is of the same order as the deviation due to different time step size. Finally, it should be noted that for the presented ranges of time step size, grid resolution and spin domain size, the spin domain size has the largest influence on the delivered power.

4.2. Pitch deflection

Since each propeller is operating at constant rotation rate, the right pitch deflection needs to be calculated in order to match the propeller thrust and delivered power for each condition. The delivered power is determined by computing the propeller torque for three pitch deflections, and then interpolating to the pitch deflection value that results in the right power absorption. This procedure is applied for all three blade designs. The eventual pitch deflection for each operating condition and each design is depicted in Table 6.

5. Propeller cavitation erosion risk assessment

The erosion model described in Section 2 is employed to compute the impact distribution on the propeller blades. To better resolve the cavity dynamics, a finer grid is needed, than the one used for the delivered power prediction. Therefore, an additional refinement is applied on the volume cells where the vapor volume fraction is non-zero over one full revolution. Only the volume around one blade is refined to reduce the computational cost.

First, a coarser mesh is applied to estimate the maximum vapor fraction in each cell over one propeller revolution. Based on that, a refinement is applied on one of the blades, at each location where the maximum vapor fraction is non-zero. The grid and time step size follows the best practice guidelines as proposed in previous work (see Melissaris et al. (2020)), thus approximately 20 cells along the smallest dimension of the vapor cavity, at its maximum size, and 40 time steps during the collapse, based on the Rayleigh–Plesset collapse time. For a cavity with diameter $D \approx 45$ mm (see Fig. 9), this translates to a minimum cell size of $c \approx 2.25$ mm, and a time step size of $\Delta t = 6.13 \times 10^{-4}$ s or a rotation rate of 0.085 deg per time step. Table 7 shows the eventual number of cells per cavity width, when the cavity is at its maximum size, for each grid, excluding the number of the prism layers close to the wall. A wall resolved approach is used to better control the
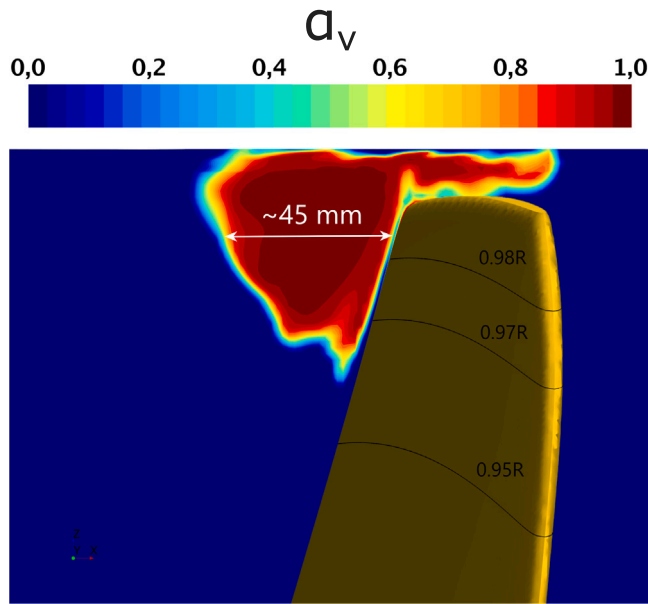
Fig. 9. Maximum vapor volume fraction over one full propeller revolution. The cross section is showing the approximate maximum size of the shed cavity.
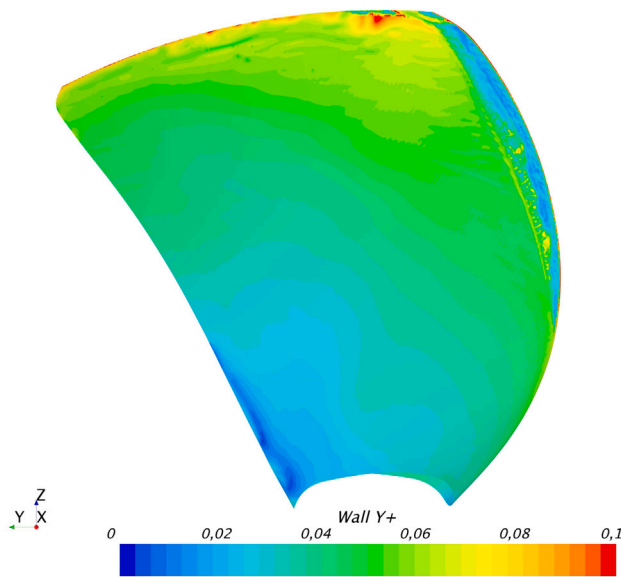

Fig. 10. Wall y+ distribution on the blade for Grid 2.

grid similarity for different grid densities. The wall y^+ values on the blade are well below 0.1 even for the coarsest grid (see Fig. 10). The developed vapor volume on the original blade is depicted in Fig. 11, for the ballast minimum load condition, indicating the cavity size and dynamics. The shed cavity shown at 330 deg blade position has already collapsed at top blade position, while the width of the main sheet cavity has been significantly reduced. Furthermore, a representation of the mesh, after applying the refinement, is shown in Fig. 12.

A convergence criterion, r, is employed to ensure the iterative convergence during each time step. The criterion is satisfied when the deviation between the maximum and the minimum value of the total vapor volume fraction, α_v, over the last n iterations, divided by the

Table 7
Mesh information for three different grids, showing the total number of volume cells, surface cells on the refined blade, prism layers, and cells per cavity width along the maximum cavity size.

Grid	# cells total	# cells on refined blade	# prism layers	# cells per width at maximum cavity size
Grid 1	7.37 M	102.9 k	13	19
Grid 2	11.03 M	142.8 k	16	24
Grid 3	18.70 M	232.0 k	20	30

average of α_v over the last n iterations is lower than 10^{-6}:

$$r = \frac{|\ max\{\alpha_v\}^i_{j=i-n+1} - min\{\alpha_v\}^i_{j=i-n+1}\ |}{\frac{1}{n}\sum_{j=i-n+1}^{i}\alpha_{v_j}} < 10^{-6} \qquad (27)$$

where $i \ >= \ 5$ the iteration number during the time step. In all simulations, a value $n = 5$ is set, which always results in a reduction of the residual of the vapor volume transport equation at least below 10^{-6}.

5.1. Original design

5.1.1. Sensitivity study

A sensitivity study is conducted for the original blade at the ballast condition, so that a time step and grid size independent solution is obtained for the cavity impact distribution on the blade (blade impact distribution). First, the blade impact distribution is computed for Grid 2 and rotation rates, 0.1, 0.08 and 0.06 deg per time step. Fig. 13, depicts the total accumulated surface energy on the blade per rotation, without energy focusing, for 5 propeller revolutions, and three different time step sizes. A very small decrease in the surface impact energy is observed for smaller time step sizes, as a result of the shift in collapse locations. Large time step sizes could lead to delayed collapse times, which affect the locations where energy will be radiated. For a cavity to collapse at a different location means different driving pressure. When there is a delay in collapse, the collapsing cavity is more likely to be advected towards stronger pressure gradients, resulting in a more violent collapse, and higher amount of radiated energy. Therefore, we should always expect higher magnitude of radiated energy for large time step sizes.

Different collapse locations also affect the projection of the radiated energy, since the distance and orientation from the surface changes. If the energy is radiated above an infinite and flat surface, the overall amount of surface energy should be independent of the collapse location. However, the propeller blade has a finite and curved surface, and therefore the total amount of surface impact energy should depend on the collapse location. For the non-focusing approach this effect is not that pronounced, since the energy is continuously being radiated during negative volume change, and the shift in locations where energy is radiated is not that big.

On the other hand, the sensitivity is higher when energy focusing is applied (see Fig. 14), and the amount of energy projected onto the blade surface is more sensitive to the location of the final collapse. In the focusing approach, the entire collapse energy is radiated from a very confined volume, the collapse center. Consequently, the shift in the location of radiation sources can be very large, and therefore a much larger impact on the surface energy distribution should be anticipated.

Furthermore, since the time step sizes have been selected so that we can resolve the larger structures that are shed from the sheet cavity, the sensitivity on the surface accumulated energy should be larger at
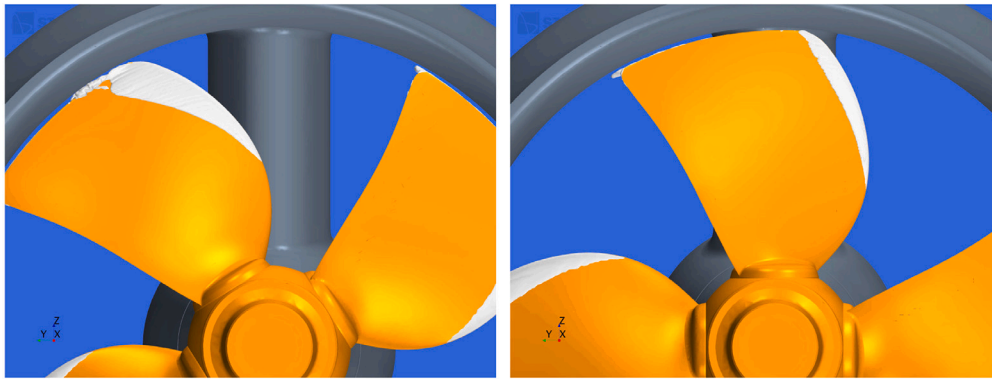
Fig. 11. Total vapor volume on the original blade at 330 deg (left) and top (right) position, in ballast minimum load condition.
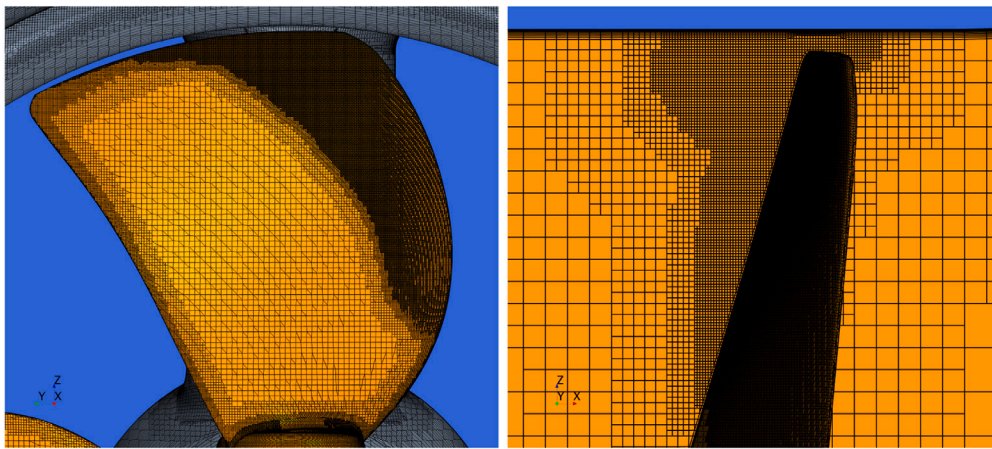

Fig. 12. Mesh representation of the refined blade for the original blade, showing the additional refinement to capture the cavity dynamics.

locations of smaller collapsing cavities, which are not fully resolved. For instance, even the smallest time step size might not be sufficient to resolve the small cavities that are shed at the trailing edge of the sheet cavity, leading to a larger overall sensitivity of the total accumulated energy on the blade. Achieving an absolute time step size independent solution with energy focusing might require extremely smaller time step sizes, and consequently a compromise needs to be made between accuracy and computational effort. Since our main goal here is to mainly resolve the larger scales and the collapse of the bigger cavities during each propeller revolution, a time step size lower than 0.1 deg per time step is considered sufficient.

Finally, we also observe some deviation between the total surface impact energy for the same time step size and different propeller revolutions. Nevertheless, those differences are mainly related to system instabilities of cloud cavitation, and in particular the instability of the stagnation point at the closure of the sheet cavity (Franc and Michel, 2004; Melissaris et al., 2020).

Now, looking at the impact distribution on the blade surface, for the non-focusing approach, and different grid densities, a grid independent solution is achieved for the different meshes, as shown in Fig. 15. The time step size is modified for each mesh based on the refinement ratio h_i/h_3 (see Table 5). On the other hand, when the kinetic energy focusing is applied, the accumulated energy on the blade is more sensitive to the grid resolution. Insufficient spatial resolution can lead to early collapse of cavitating structures, leading to the opposite effect than insufficient time step size. The final stage of the collapse takes place at locations, which either are further away from the surface, or experience weaker pressure gradients and consequently smaller amounts of energy are radiated. For the original propeller design, and the ballast condition
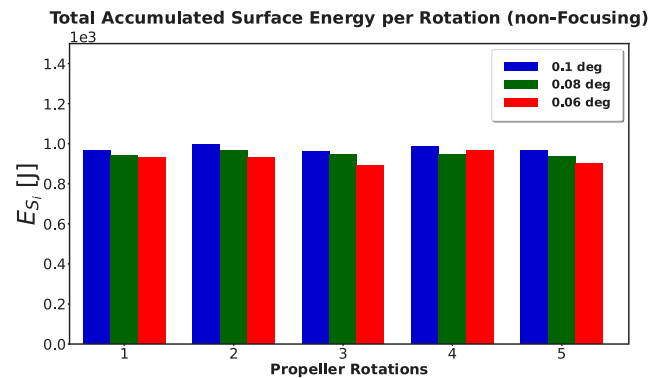

Fig. 13. Total accumulated surface energy per propeller rotation on Grid 2, for five consecutive revolutions, for three different time step sizes, using the non-focusing model.

a higher accumulated surface energy is predicted for finer grids (Grid 2 and 3) as shown in Fig. 16.

The impact distributions on the refined blade, after five propeller revolutions, for each grid, are illustrated and compared in Fig. 17. The high energy density areas are mainly located close to the tip, and towards the mid-chord region. Although the same impact locations are predicted for all grids, the magnitude of the accumulated surface specific energy is slightly lower for the coarser mesh, both with and without energy focusing. In addition, small differences are observed on the energy distribution close to the tip, between Grid 2 and 3, however, these differences are probably related to the higher grid resolution,
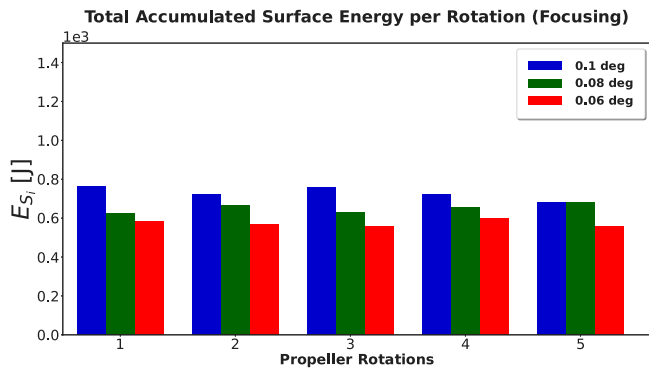
Fig. 14. Total accumulated surface energy per propeller rotation on Grid 2, for five consecutive revolutions, for three different time step sizes, using the focusing model.
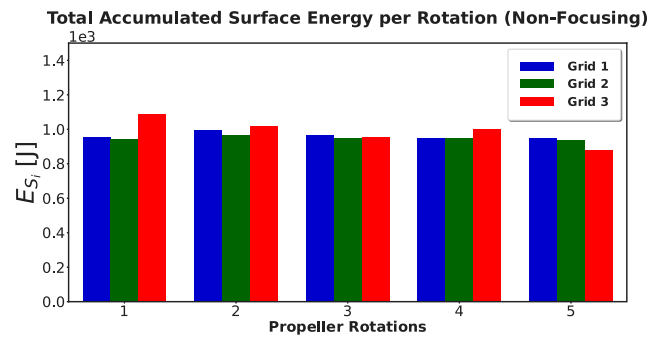

Fig. 15. Total accumulated surface energy per propeller rotation, for five consecutive revolutions, for three different grid densities, using the non-focusing model.
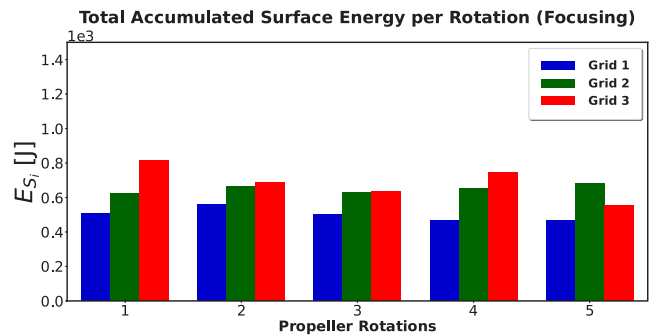

Fig. 16. Total accumulated surface energy per propeller rotation, for five consecutive revolutions, for three different grid densities, using the focusing model.

Fig. 17. Surface specific accumulated energy on the refined propeller blade, obtained from the non-focusing and the focusing model after five propeller revolutions, for Grid 1 (left), Grid 2 (middle), and Grid 3 (right).

since the total accumulated energy is similar. As the grid resolution increases, more details are captured in the flow, and a higher amount of secondary flow is resolved. That results in accurately resolving the collapse of smaller and smaller structures, and therefore some small deviations in the impact distributions are expected.

Finally, comparing the distributions with and without energy focusing, we notice that the radiated energy is accumulated in larger areas on the blade, if we do not apply the energy focusing model. Since energy is radiated instantaneously, as the cavity volume is decreasing, the energy is continuously being distributed, leaving a footprint along the sheet cavity trailing edge. On the other hand, the energy is more scattered and localized with the energy focusing model. The energy is focused into smaller volumes, towards the collapse center, and thus, at the final stage of the collapse, the radiated energy is accumulated in smaller areas on the blade, especially when the collapse center is close
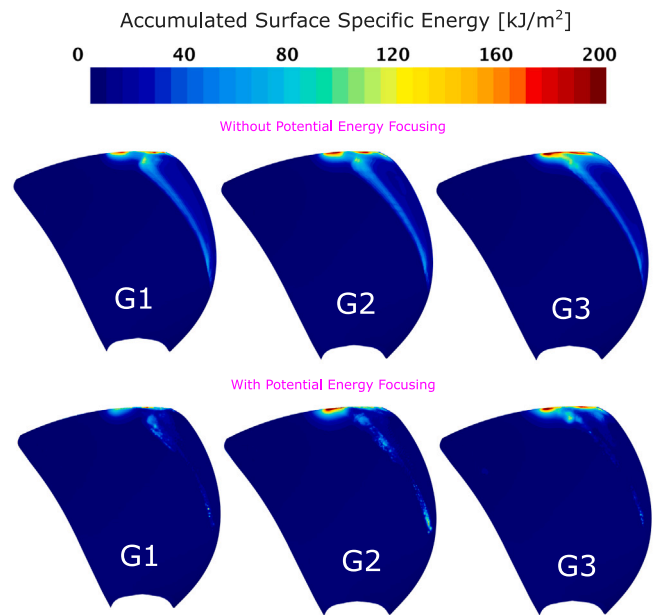
to the surface. For implosions at larger distances, the energy impact distribution can be very similar with both methods.

5.1.2. Other operating conditions

A representation of the developed vapor volume on the original blade, when it is at the top position, is depicted in Fig. 18 for the minimum towing, and dynamic positioning condition. The total accumulated surface energy per propeller rotation for all three operating conditions for Grid 2 and a time step size of 0.08 deg per time step is shown in Figs. 19 and 20, without and with energy focusing respectively. In minimum towing condition, the cavity dynamics are very similar to the ballast minimum load condition, showing a slight increase in the vapor volume and consequently in the accumulated surface energy. On the other hand, in dynamic positioning, the unit clearly experiences a much higher amount of cavitation, resulting in a much larger amount of accumulated energy on the surface (about 2–2.5 times larger). It is important to note that, since the amount of vapor in both the minimum towing condition and dynamic positioning is larger than the ballast min load condition, a grid resolution as fine as in Grid 2 and a rotation rate of 0.8 deg per time step (as derived by the sensitivity study in Section 5.1.1) are sufficient to resolve the cavities of at least the same size as in the ballast minimum load condition.

Comparing the total accumulated surface energy between the non-focusing and focusing model, it is again observed that a larger amount of surface energy is predicted when there is no energy focusing. That is because of the instantaneous release of energy in case of a negative volume change. Thus, cavities that are subjected to negative volume change, but either never collapse or collapse far away from the surface, will leave a substantial energy footprint on the surface, while that will not occur when energy focusing is applied. That becomes even more obvious when looking at the distribution of the surface specific energy on the original blade after 5 propeller revolutions, without (Fig. 21) and with energy focusing (Fig. 22). The non-focusing model is predicting larger amount of surface energy both at the trailing edge of the developed sheet cavity, and at the location of the main impact originated from the cloudy structures shed from the sheet cavity.

Furthermore, the energy distributions for the ballast and the towing condition are very similar, as it was already indicated by the total
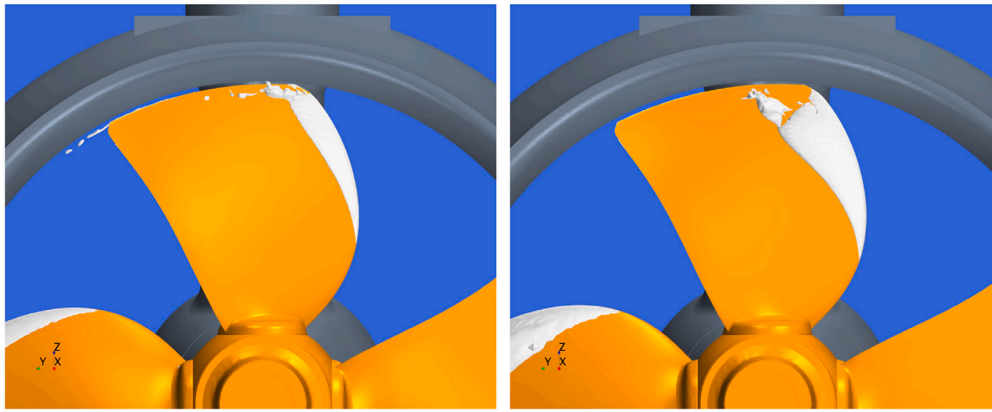
Fig. 18. Total vapor volume when the blade is at the top position, for minimum towing (left), and dynamic positioning condition (right).
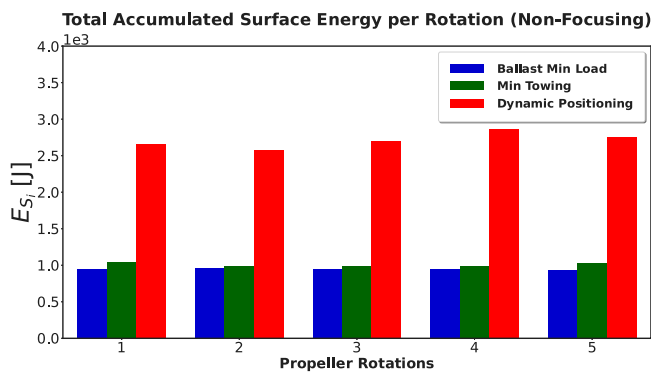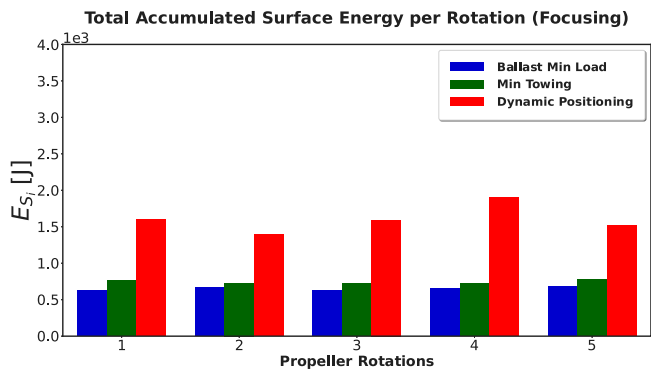

Fig. 19. Total accumulated surface energy per propeller rotation, for five consecutive revolutions, for ballast minimum load (blue), minimum towing (green), and dynamic positioning condition (red), using the non-focusing model. (For interpretation of the references to color in this figure legend, the reader is referred to the web version of this article.)

Fig. 21. Surface specific accumulated energy on the refined propeller blade, obtained from the non-focusing model after five propeller revolutions, for ballast minimum load (left), minimum towing (middle), and dynamic positioning condition (right).

Fig. 20. Total accumulated surface energy per propeller rotation, for five consecutive revolutions, for ballast minimum load (blue), minimum towing (green), and dynamic positioning condition (red), using the focusing model. (For interpretation of the references to color in this figure legend, the reader is referred to the web version of this article.)

Fig. 22. Surface specific accumulated energy on the refined propeller blade, obtained from the focusing model after five propeller revolutions, for ballast minimum load (left), minimum towing (middle), and dynamic positioning condition (right).

accumulated surface energy. However, in the ballast condition, most of the surface energy is accumulated closer to the tip and more towards the mid-chord, which is probably related to the difference in inflow speed, resulting in slightly different angles of attack of the incoming flow. In dynamic positioning the accumulated energy on the blade is clearly much larger, and it is distributed over a larger blade area.

Looking at the energy distribution for each condition, it is easy to distinguish the amount of the accumulated energy, however, it is not
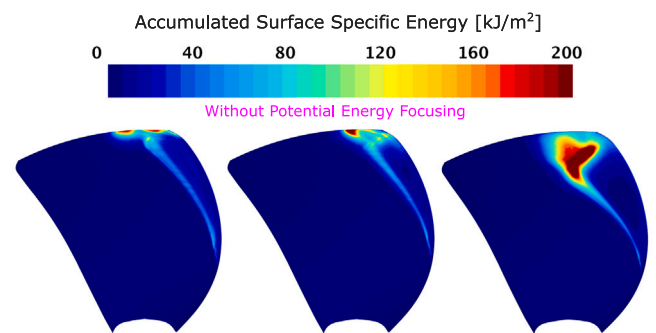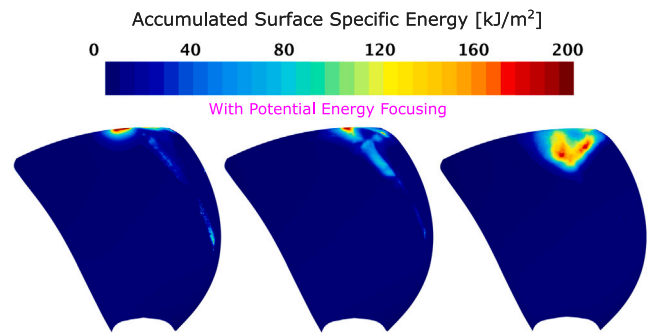
trivial to identify whether higher energy content means also higher risk for erosion. To get a better impression of the flow aggressiveness and the extent of the impacted area, a more quantitative analysis of the damage in the impacted areas is needed. Figs. 23 and 24 give the surface specific energy over the percentage of the impacted blade area. Such a plot shows the amount of energy distributed over a certain amount of area on the blade. These representations give a better insight into the erosion risk of the impacted areas on the blade. Areas with high surface specific energy have an increased probability to experience erosion and material loss. Based on such analysis, a more quantitative comparison is possible between the different conditions, as well as the different propeller designs.

Comparing Figs. 23 and 24 it is noteworthy that the energy is evenly distributed for all three conditions if the non-focusing model is used,
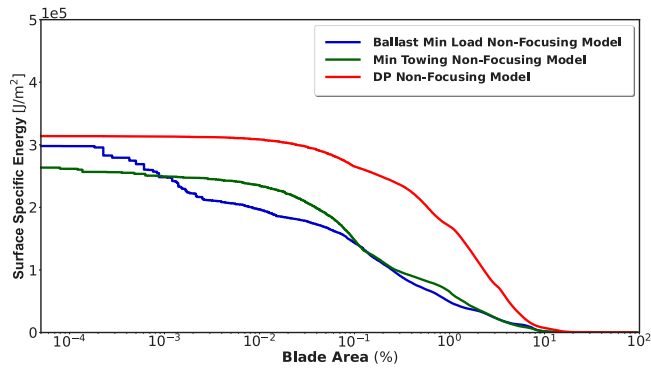
Fig. 23. Surface specific energy over the blade area, showing the extent and the percentage of the impacted blade area, after five propeller revolutions, for the non-focusing model.
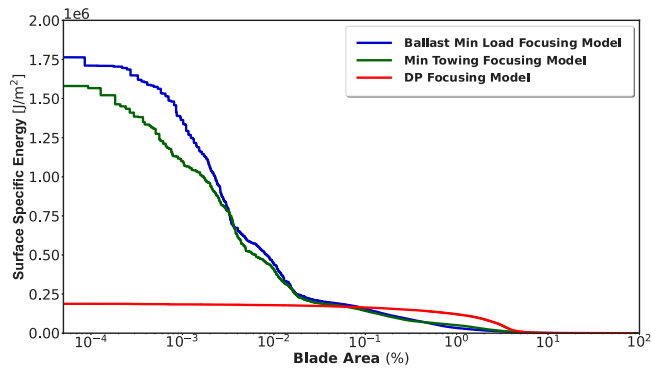

Fig. 24. Surface specific energy over the blade area, showing the extent and the percentage of the impacted blade area, when the energy focusing approach is employed.
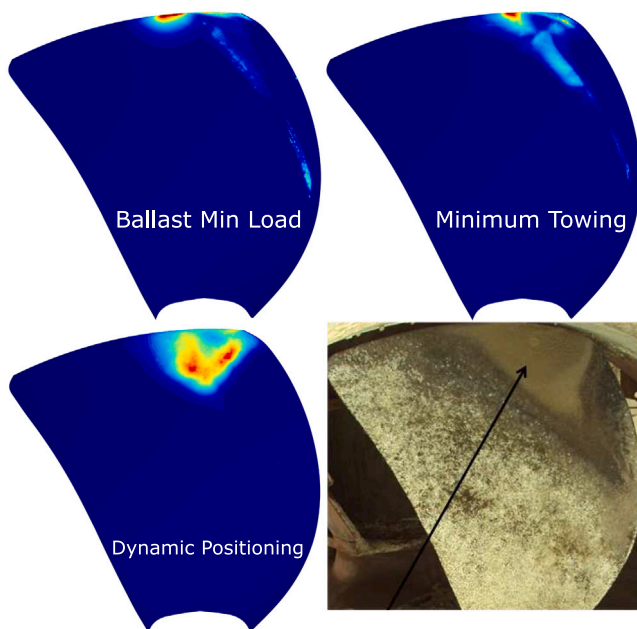

Fig. 25. Comparison of the erosion risk predicted by CFD with the focusing model for the three operating conditions and the real erosion on the original blade.

while more extreme events can be identified with the energy focusing approach. That is only the case for the ballast and towing condition, since in DP the energy remains evenly distributed over a larger area
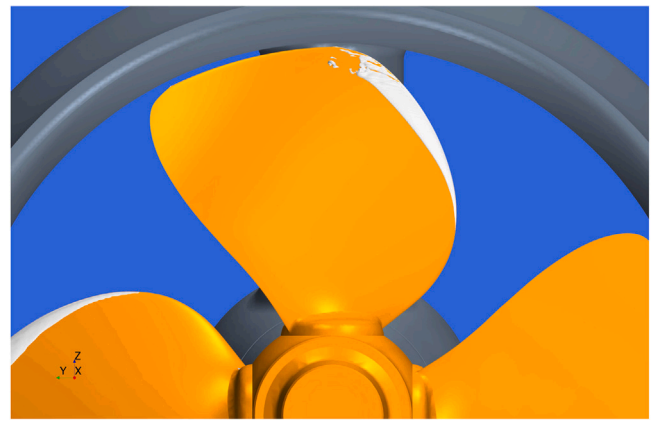

Fig. 26. Representation of the total vapor volume on the refined blade of the first redesign, in dynamic positioning.
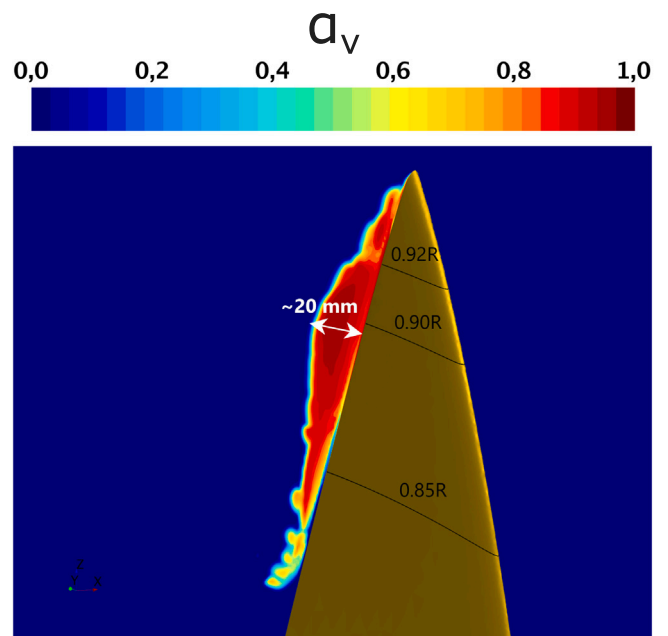

Fig. 27. Maximum vapor volume fraction over one full propeller revolution. The cross-section is showing the approximate maximum size of the shed cavity.

even with the focusing model (see Fig. 24). This possibly indicates that the collapse of the main cloudy structures shed from the developed sheet cavity, during each cycle, collapse further away from the surface resulting in a surface impact of larger area and lower magnitude. That leads to an energy impact distribution similar to the one obtained from the non-focusing model.

Looking at the magnitude of the surface specific energy, obtained from the focusing model, the cavity dynamics during the ballast condition seem to be the most aggressive ones, indicating slightly higher erosion risk than the towing condition. On the contrary, in dynamic positioning, even though the total accumulated energy is much larger than in the other two conditions, the energy is evenly distributed over a much larger area, indicating a much lower erosion risk. Nevertheless, when we compare the energy distribution obtained by CFD, with the actual erosion on the original blade (see Fig. 25), we can clearly see that the actual erosion on the real blade is a result of the combined impacts originated form all three operating conditions.

Based on the CFD analysis, in the ballast and minimum towing condition, the highest erosion risk area is close to the tip. Indeed,
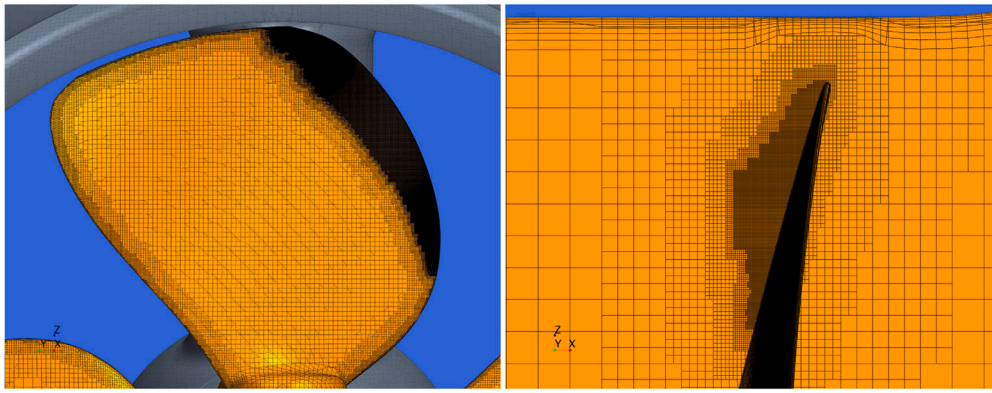
Fig. 28. Mesh representation on the refined blade for the first redesign, showing the additional refinement to capture the cavity dynamics.
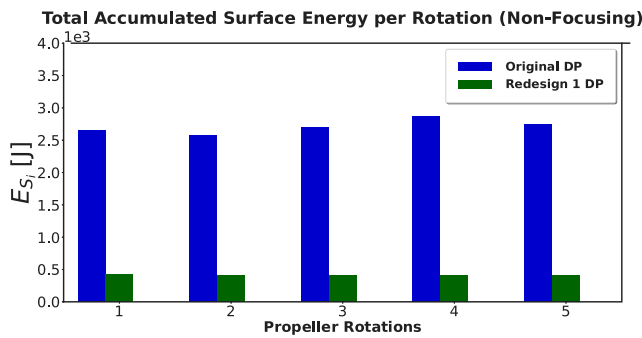

Fig. 29. Total accumulated surface energy per propeller rotation for five consecutive revolutions, for the original blade and the first re-design, in dynamic positioning, using the non-focusing model.
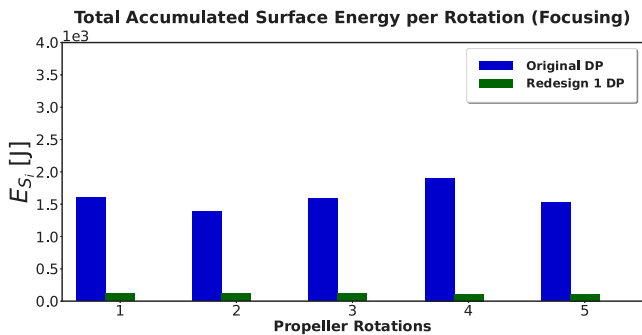

Fig. 30. Total accumulated surface energy per propeller rotation for five consecutive revolutions, for the original blade and the first re-design, in dynamic positioning, using the energy focusing model.

Fig. 31. Surface specific accumulated energy on the refined propeller blade of the original propeller (left) and the first re-design (right), obtained from the non-focusing (top) and the focusing model (bottom) after five propeller revolutions.
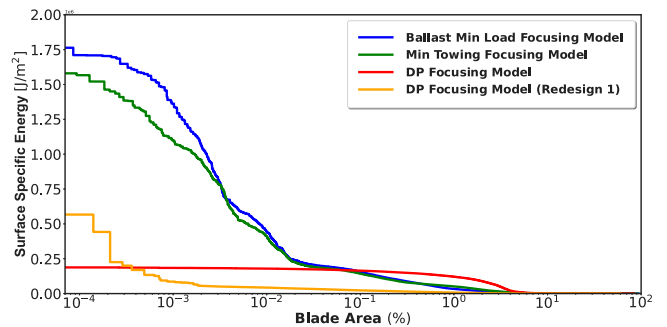
Fig. 32. Surface specific energy over the blade area, showing the extent and the percentage of the impacted blade area, for the original blade in all three operating conditions, and the first re-design in dynamic positioning, after five propeller revolutions, using the energy focusing model.

looking at the actual erosion on the real blade, severe erosion is identified close to the tip, matching well with the CFD locations. On the other hand, the eroded area on the real blade extends to lower radii, while very little energy was found from the computations at lower radii for these two conditions. Therefore, it is concluded that erosion is also likely to occur when the vessel is operating in DP. Even though a low magnitude of surface specific energy is predicted for this condition, and the energy is evenly distributed over a large area of the blade, this amount of energy still seems to be sufficient to cause erosion.

One of the long lasting debates about cavitation erosion is whether common erosion on the blades occurs due to extreme events of low frequency or due to repetitive events of lower magnitude, but of higher frequency. The implosion loads reproduced during the ballast and towing condition can be characterized as extreme events due to
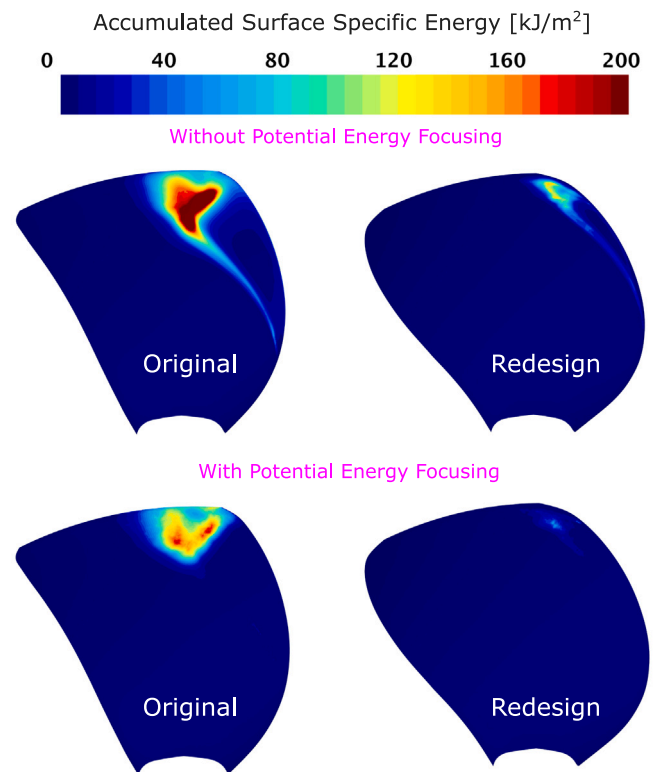
Fig. 33. Comparison of the erosion risk predicted by CFD with the focusing model for the first re-design in dynamic positioning, and the real erosion on the actual re-design.

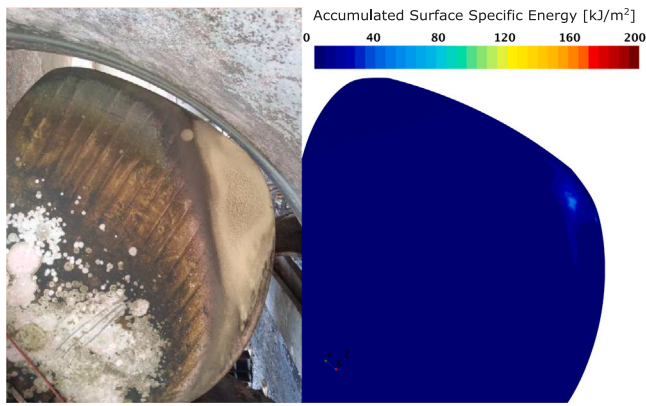their high energy content, which is distributed over smaller areas. The location of the implosion might differ from cycle to cycle, and therefore the frequency of the impact on each fixed location of the blade is lower than the BPF. On the other hand, the impact exerted by the implosion loads during dynamic positioning, can be considered as repetitive events of lower amplitude. In this case the frequency of the impact at a fixed location can be much higher since the energy is evenly distributed over a larger area. From the actual erosion on the real blade, it seems that both cases are qualified to cause erosion and material loss. So, in the case where the frequency of an implosion at a fixed location is high enough, it seems that it can cause erosion even though the exerted stress at that location does not exceed the material yield stress (similar to fatigue).

Finally, there is still the possibility that the implosion loads exerted on the surface during dynamic positioning condition are still exceeding the material yield strength, causing plastic deformation. In such a case, the implosion loads during the other two conditions, should be even higher, resulting in more severe erosion close to the tip. Looking at the actual blade, the erosion at the tip seems slightly more severe than in lower radii, however it is not as obvious, and makes it difficult to explain such big differences in the magnitude of the implosion loads.

5.2. First re-design

Since extensive erosion occurred on the original blade, a new propeller design was made to mitigate pressure side cavitation erosion, without compromising in performance and thruster efficiency. Indeed, in ballast minimum load and minimum towing condition, propeller cavitation on pressure side was significantly reduced, showing no potential of cavitation erosion. However, a serious amount of cavitation was predicted in dynamic positioning (see Fig. 26), and therefore the erosion model was applied to estimate the erosion risk on the first re-design.

In a similar way as for the original design, a new volume refinement is applied around one of the blades, on the cells where the vapor volume is non-zero over one full revolution. For a cavity with a maximum width $D \approx 20$ mm (see Fig. 27), a minimum cell size of $c \approx 1$ mm, and a time step size of $\Delta t = 2.32 \times 10^{-5}$ are suggested by previous studies (Melissaris et al., 2020). This is translated to about 20 cells over the maximum cavity width. Based on the results of the original design, a slightly finer grid is required (24 cells per cavity width were used in Grid 2). Therefore, a minimum cell size of $c \approx 0.8$ mm, and a time step size of $\Delta t = 1.86 \times 10^{-5}$ are eventually used, resulting in 25 cells per cavity width (excluding the prism layer cells). Fig. 28 depicts the mesh representation on the refined blade.

The total accumulated surface energy on the refined blade, when the vessel is operating in dynamic positioning, is compared between the original design and the first re-design, without (Fig. 29) and with (Fig. 30) energy focusing, for a simulation time of 5 propeller revolutions. First, the total accumulated surface energy for the original design shows higher deviation during each revolution. These differences come mainly from the intrinsic instabilities of the partial cavity (Franc and Michel, 2004). The larger amount of vapor and the stronger dynamics in DP are strengthening the instabilities, causing larger deviations between each propeller revolution.

Furthermore, The accumulated energy on the original blade is much larger than the accumulated energy on the re-design, especially when energy focusing is used. This is caused by the much larger vapor volume we observe at the same condition as for the original blade. We notice the same, when looking at the surface impact distribution (see Fig. 31). A much larger area is impacted on the original blade, while the accumulated energy and the impacted area are much smaller on the first re-design. However, as already mentioned, this does not necessarily mean that the risk for erosion on the original blade is higher than on the re-design.

To get a better insight into the high erosion risk areas, we should have a look at the surface specific energy. Fig. 32 presents the magnitude of the surface specific energy over the percentage of area, on which the energy is distributed, when energy focusing is applied. Comparing the impacted area between the original design and the first re-design, in the dynamic positioning condition, we see that a much larger area is impacted on the original blade. On the other hand, there is a small area on the blade of the re-design where more energy is accumulated. This indicates a higher risk of erosion for the re-design, even though the vapor volume is much smaller. This numerical finding is confirmed by the actual damage on the real blade of the re-design. Fig. 33 shows that severe erosion occurs at the location where high surface specific energy is predicted. Looking only at the surface impact distribution, we could consider a very low risk of erosion. However, the high surface specific energy indicates a high risk of erosion, which corresponds well with the actual damage location. The difference in affected surface area may be explained by the lack of statistics on the surface impact obtained from the simulations.

5.3. Second re-design

Cavitation analysis on the second re-design, in all three operating conditions, showed very little cavitation on the pressure side. Even in dynamic positioning, only a small amount of cavitation is predicted at the leading edge. Looking at the actual erosion on the real blade (see Fig. 34), cavitation erosion occurred further away from the leading edge, indicating more extensive cavitation on the blades than what we could expect from the simulations. Therefore, we can hypothesize that, especially in this case, including the ship hull will have a significant impact on the propeller wakefield, resulting in a different inflow compared to the one used in the simulations. The presence of the hull results in a highly inclined flow towards the upcoming blade, leading to higher angles of attack, and consequently more cavitation dynamics.

Indeed, Fig. 35 shows the vapor volume on the second redesign at an inclined inflow of 15 degrees, 7 knots speed, and a pitch deflection similar to the one in dynamic positioning. Clearly, a larger amount of vapor volume is simulated, and especially on the upcoming blade. A vary thin sheet cavity is observed, which is shed to smaller structures, that possibly collapse at locations close to the actual damage on the real blade. Therefore, it is possible to simulate larger amount of vapor volume on the blade, but at an operating condition different than the ones reported as critical for cavitation erosion in Table 6.

Finally, water quality and roughness can play a major role in cavitation inception and cavity dynamics. In all the simulations performed, a perfect liquid and water quality is assumed, while all surfaces are
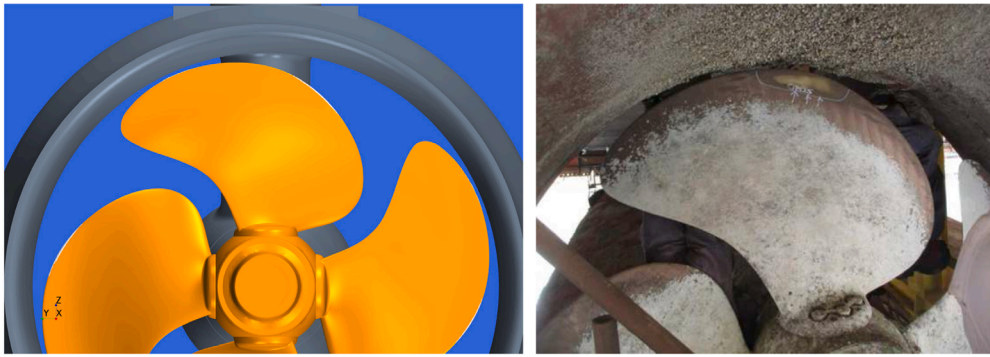
Fig. 34. Representation of the vapor volume on the blades of the second re-design, in dynamic positioning (left), and the actual damage on the real blade (right).

Fig. 35. Representation of the vapor volume on the blades of the second re-design, at 7 knots, with incoming flow at 15 deg angle to emulate the flow behind the ship hull.

perfectly smooth, possibly influencing the cavitation development and the impact distribution to some extent.

6. Conclusion

A novel erosion model has been used for the first time to predict propeller cavitation erosion on ship scale. An erosion risk assessment has been performed on a full scale steerable thruster in open water configuration, in three different operating conditions, and three different propeller designs.

To compute the fraction of radiated energy (originating form the collapse of cavitating structures) on the impacted surface, a fully continuous form of the solid angle is used. The exact solid angle of a surface element, i.e. a surface face, depends on the face topology and requires specific algebraic formulas. If the topology of the surface face is unknown or if the topology is known, but the exact surface angle involves algebraic expressions that are difficult to evaluate, one might employ an approximation of the solid angle that only depends on the surface area of the face, its normal vector, and the distance vector between face center and the point of wave radiation. This approximation often leads to significant errors for sources located very close to the surface. Bounding the solid angle to the maximum solid angle for such cases, reduces the approximation error to its minimum.

A sensitivity study has been performed on the magnitude of the total accumulated surface energy on the propeller blade, during each propeller revolution. When energy focusing is applied, the grid and time step sensitivity is larger than without energy focusing, due to the larger influence of the shift in the collapse location on the projected

surface energy. However, 24 cells per initial cavity width, and a time step size that corresponds to at least 40 steps per cavity collapse time are considered sufficient to resolve at least the larger structures that are shed from the developed sheet cavity on the pressure side of the blade (the collapse time can be estimated from the Rayleigh–Plesset collapse time of a spherical cavity with diameter equal to the maximum width of the sheet cavity on the blade).

When the blade impact distribution is assessed without energy focusing, the predicted accumulated surface energy is much higher than the one predicted with energy focusing, while it extends over a larger surface area, even larger than the actual impacted area on the real blade. At the same time, the surface specific energy is lower, leading to smaller magnitudes of the maximum loads on the surface. Due to the continuous release of energy at any moment there is a negative volume change, the non-focusing approach fails to predict the right amount of radiated energy at the right locations. Consequently, energy focusing is essential for an accurate prediction of the instantaneous impact loads and their distribution on the blades.

The capability of the erosion model to estimate the implosion loads and their potential damage on the blade surface is demonstrated for different conditions and different designs. The surface specific energy distribution provides good information about the erosion risk over the blade area, where large amounts of accumulated energy indicate a high risk for erosion. Comparison of the computed blade impact distribution with the actual damage on the blade, showed, for two propeller designs, a very good agreement between the high erosion risk areas, as predicted by the energy focusing model, and the actual damage location. A third propeller design showed less cavitation at the critical operating conditions than what the actual erosion indicates. This is hypothesized to be due to the difference in the wakefield with and without the hull. Highly inclined flow, as if the unit was operating behind the hull, showed, at certain condition, an increase in the vapor volume on the blades.

Finally, we show that the energy focusing model is suitable for identifying different cavitation aggressiveness levels, based on the operating condition and the blade design. Based on the analysis of the surface specific energy, the highest erosion risk was found on the original blade, in ballast minimum load, and minimum towing condition. A very slight amount of cavitation was found on the blades of the first re-design, and therefore no erosion risk for these two conditions. On the other hand, in dynamic positioning, the surface specific energy on the first re-design indicated higher risk than on the original blade. Insufficient cavitation was found on the second re-design, for the given operating conditions, to allow for erosion risk assessment. This lack of predicted cavitation dynamics is credited to the neglect of the presence of the hull.

CRediT authorship contribution statement

Themistoklis Melissaris: Conceptualization, Methodology, Software, Investigation, Validation, Writing – original draft. **Sören Schenke:** Conceptualization, Methodology, Writing – review & editing. **Norbert Bulten:** Writing – review & editing. **Tom J.C. van Terwisga:** Conceptualization, Supervision, Writing – review & editing.

Declaration of competing interest

The authors declare that they have no known competing financial interests or personal relationships that could have appeared to influence the work reported in this paper.

Acknowledgments

References

Arecchi, A.V., Messadi, T., Koshel, R.J., 2007. Field Guide to Illumination. SPIE Press, Bellingham, WA.

Carlton, J., 2019. Marine Propellers and Propulsion. Butterworth-Heinemann, Kidlington, Oxford.

Chahine, G.L., Franc, J.-P., Karimi, A. (Eds.), 2014. Advanced Experimental and Numerical Techniques for Cavitation Erosion Prediction, first ed. In: Fluid Mechanics and Its Applications, vol. 106, Springer, Dordrecht, pp. 3–180.

Flageul, C., Fortes-Patella, R., Archer, A., 2012. Cavitation Erosion Prediction by Numerical Simulations. In: Proceedings of the 14th International Symposium on Transport Phenomena and Dynamics of Rotating Machinery, Honolulu, HI, USA.

Fortes-Patella, R., Challier, G., Reboud, J.L., Archer, A., 2013. Energy balance in cavitation erosion: From bubble collapse to indentation of material surface. J. Fluids Eng. 135 (1), 011303.

Fortes-Patella, R., Reboud, J.L., 1998. A new approach to evaluate the cavitation erosion power. J. Fluids Eng. 120 (2), 335–344.

Franc, J.P., Michel, J.M., 2004. Fundamentals of Cavitation. Kluwer Academic Publishers, Dordrecht.

Gotoh, H., Yagi, H., 1971. Solid angle subtended by a rectangular slit. Nucl. Instr. Meth. 96, 485–486.

Hammit, F., 1963. Observations on cavitation damage in a flowing system. J. Basic Eng. 85 (3), 347–356.

Leclercq, C., Archer, A., Patella, R.F., Cerru, F., 2017. Numerical cavitation intensity on a hydrofoil for 3d homogeneous unsteady viscous flows. Int. J. Fluid Mach. Syst. 10 (254).

Melissaris, T., Bulten, N., van Terwisga, T.J.C., 2019. On the applicability of cavitation erosion risk models with a urans solver. J. Fluids Eng. 141 (101104).

Melissaris, T., Schenke, S., Bulten, N., van Terwisga, T.J.C., 2020. On the accuracy of predicting cavitation impact loads on marine propellers. WEAR 456–457 (203393), http://dx.doi.org/10.1016/j.wear.2020.203393.

Menter, F., 1994. Two-equation eddy-viscosity turbulence modeling for engineering applications. AIAA J. 32, 1598–1605.

Obreschkow, D., Kobel, P., Dorsaz, N., de Bosset, A., Nicollier, C., Farhat, M., 2006. Cavitation bubble dynamics inside liquid drops in microgravity. Phys. Rev. Lett. 97 (094502).

Oosterom, A.V., Strackee, J., 1983. The solid angle of a plane triangle. IEEE Trans. Biomed. Eng. 2 (BME-30), 125–126.

Patankar, S., 1980. Numerical Heat Transfer and Fluid Flow. Hemisphere Publishing Corporation, New York.

Peters, A., Lantermann, U., el Moctar, O., 2018. Numerical prediction of cavitation erosion on a ship propeller in model- and full-scale. Wear 408–409, 1–12.

Ponkratov, D., 2015. DES prediction of cavitation erosion and its validation for a ship scale propeller. J. Phys. Conf. Ser. 656 (012055).

Ponkratov, D., Caldas, A., 2015. Prediction of Cavitation Erosion by Detached Eddy Simulation (Des) and Its Validation Against Model and Ship Scale Results. In: Proceedings of the 4th International Symposium on Marine Propulsors, Austin, Texas, USA.

Rowlands, G., 1961. Solid angle calculations. Int. J. Appl. Radiat. Isot. 10, 86–93.

Schenke, S., 2020. Cavitation Implosion Loads from Energy Banalnce Considerations in Numerical Flow Simulations (Ph.D. thesis). Delft University of Technology, Delft, The Netherlands.

Schenke, S., Melissaris, T., van Terwisga, T.J.C., 2019a. On the relation between the potential cavity energy and the acoustic power signature caused by periodic vapor cavity collapses. In: Proceedings of the 6th International Symposium on Marine Propulsors, Rome, Italy.

Schenke, S., Melissaris, T., van Terwisga, T.J.C., 2019b. On the relevance of kinematics for cavitation implosion loads. Phys. Fluids 31, 052102.

Tinguely, M., Obreschkow, D., Kobel, P., Dorsaz, N., de Bosset, A., Farhat, M., 2013. Energy partition at the collapse of spherical cavitation bubbles. Phys. Rev. E 86 (046315).

Vogel, A., Laterborn, W., 1988. Acoustic transient generation by laser-produced cavitation bubbles near solid boundaries. J. Acoust. Soc. Am. 84 (2), 719–731.

Welford, B., 1962. Note on a method for calculating corrected sums of squares and products. Technometrics 4 (3), 419–420.